

# Tropical low formation during the Australian monsoon: the events of January 2013

Roger K. Smith<sup>1</sup>, Michael T. Montgomery<sup>2</sup>, Gerard Kilroy<sup>1</sup>,  
Shengming Tang<sup>3</sup>, and Sebastian K. Müller<sup>1</sup>

<sup>1</sup> Meteorological Institute, Ludwig-Maximilians University of Munich, Munich, Germany

<sup>2</sup> Dept. of Meteorology, Naval Postgraduate School, Monterey, CA, USA

<sup>3</sup> State Key Laboratory for Disaster Reduction in Civil Engineering, Tongji University, Shanghai, China

(Manuscript received March 2015; accepted October 2015)

An analysis of tropical low formation in the Australian monsoon during January 2013 is presented based on European Centre for Medium Range Weather Forecast (ECMWF) analyses. The focus is on three lows that developed on the monsoon shear line, two of which eventually became tropical cyclones. One of the disturbances intensified as it made a loop over land. Interpretations of the formation are given in terms of vorticity dynamics. The roll up of low-level absolute vorticity associated with the shear line is a prominent feature of the early development of the lows, a mechanism akin to that believed to operate in the formation of hurricanes from Atlantic easterly waves. A notable feature of the two lows that eventually became tropical cyclones was the occurrence of persistent bouts of deep convection near the circulation centre. The development of the low that didn't achieve tropical cyclone status was apparently thwarted by strong vertical shear and drying of the middle troposphere.

## Introduction

The Australian 'Wet Season' (December-March) is characterized by a trough of low pressure lying south of the equator, the so-called monsoon trough. The trough axis coincides approximately with the "monsoon shear line", which separates westerly flow to the north from easterly flow to the south (McBride and Keenan 1982).

Early in the wet season, the trough lies over the seas to the north of the Australian continent, but later it often moves south over the continent. At any one time, the latitude of the trough axis may vary considerably with longitude. It is typical for low pressure systems to develop at spatial intervals along the trough and since water temperatures to the north of Australia can be up to 30°C, some of the lows that develop over the ocean develop into tropical cyclones. Lows that form over land are sometimes referred to as monsoon lows or monsoon depressions. These often lead to copious amounts of rainfall and may rapidly intensify into tropical cyclones if they move out to sea. In either case, these systems pose a challenge to forecasters in the region. A pioneering and insightful analysis of tropical cyclogenesis in the Australian region is provided by McBride and Keenan (1982).

While much is now known about the structure of tropical cyclones and the mechanisms by which they intensify (e.g. Montgomery and Smith 2014; Smith and Montgomery 2015), there remain gaps in understanding the mechanisms of their formation. Comparatively little is known about the structure of tropical lows over land as well as the role of deep convection in their formation and maintenance. To our knowledge, a conceptual model of these systems that might be of use to operational forecasters is not yet available. A problem is that, like tropical cyclones, the lows form over a region with relatively sparse conventional data coverage, although current numerical forecast models sometimes show considerable skill in predicting both their formation and evolution. Therefore, it may be instructive to analyze such forecasts, or better still the analyses on which the forecasts are based, as the analyses typically incorporate the observations where they are available. It is in this spirit that we examine in this paper the formation and structure of tropical lows in the Australian monsoon regime, both over land and sea, as seen by the ECMWF analyses.

## Previous studies of lows in the Australian region

Two early studies of monsoon depressions over Australia are those of Foster and Lyons (1984) and Davidson and Holland (1987). Foster and Lyons carried out a comparative study of two cloud clusters over land in the same region of northwestern Australia, one that subsequently developed into a tropical cyclone and the other that did not. While the two depressions possessed similar structures, both having deep cyclonic circulations containing deep convection and warm mid- to upper-level cores, their synoptic environments were shown to have significant differences. In particular, that of the nondeveloping system had substantial vertical wind shear compared with the system that developed.

Davidson and Holland (1987) presented an analysis of the life-cycle of two intense, heavy-rain-producing monsoon depressions over northern Australia that developed over land. They showed that the structure of Australian monsoon depressions is quite similar to those documented in the Indian region and argued that work in either region tends to be generally applicable to both regions. They found, *inter alia*, that the outer structure of these monsoon depressions is similar to that of a tropical cyclone as suggested earlier by McBride and Keenan (1982). During their most rapid deepening phases, apparent heating diagnosed from large-scale analyses was a maximum at middle levels within regions of high cyclonic vorticity. Moreover, the depressions were warm-cored through most of the troposphere; a cyclonic vorticity maximum below 850 mb changed progressively to an anticyclonic vorticity maximum near 200 mb.

## Some scientific questions

A question that immediately arises is whether the development of tropical lows that form over land is fundamentally different from that of tropical lows over the sea? Advances in understanding maritime tropical cyclogenesis emerged from seminal studies by Hendricks et al. (2004) and Montgomery et al. (2006), which pointed to the important role of rotating deep convection, and that of Dunkerton et al. (2009), who examined the nurturing role of a tropical wave and presented a new framework for describing how such hybrid wave-vortex structures develop into tropical depressions. The hybrid wave-vortex structure was likened to the development of a marsupial infant in its mother's pouch. By analogy, a juvenile proto-vortex is carried along by its parent wave until the proto-vortex is strengthened into a self-sustaining entity. For tropical storms developing within tropical waves, the recirculating flow in the wave's critical layer corresponds to the "pouch" where the wave and mean-flow speeds are similar. The centre of the pouch is defined as the intersection of the trough axis and the critical-latitude, which is oriented parallel to the easterly jet. Storm formation occurs near this so-called sweet spot. A summary of a recent field experiment designed to test the marsupial paradigm for tropical easterly wave disturbances is given by Montgomery et al. (2012). In light of the foregoing developments in cyclogenesis theory and observations, a further question arises as to whether the marsupial paradigm proves useful in understanding the formation of tropical cyclones in the monsoon regime of northern Australia, and indeed for monsoon depressions over land.

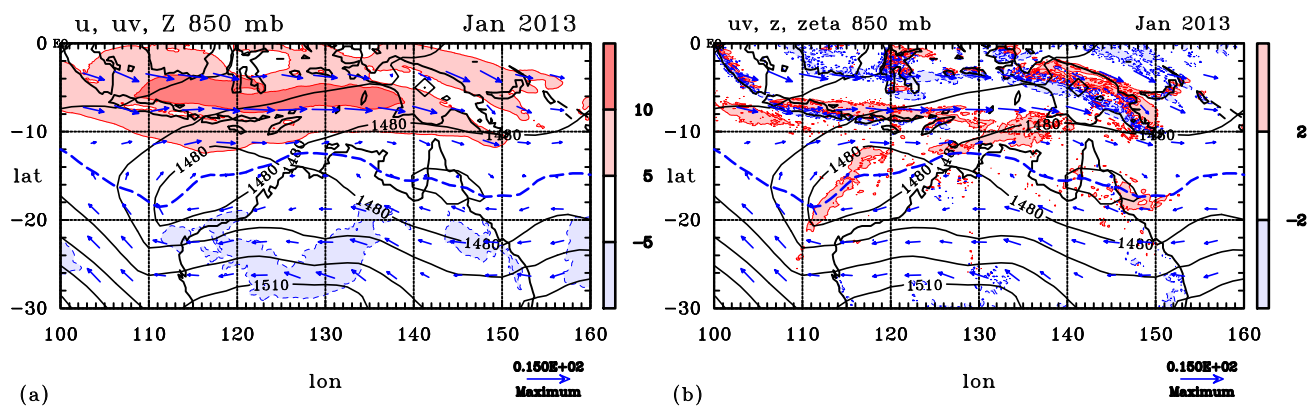
The studies by Hendricks et al. (2004) and Montgomery et al. (2006) motivated an investigation of the mechanisms of cyclogenesis in the Australian Bureau of Meteorology's Tropical Cyclone Limited Area Prediction System (TC-LAPS) (Tory et al. 2006a,b, 2007). Although the grid spacing of TC-LAPS (0.15 deg. in the horizontal) is too coarse to represent deep convection explicitly, the processes operating during cyclogenesis were found to be a coarse-grained version of those operating in the near cloud-resolving simulations by Hendricks et al. (2004) and Montgomery et al. (2006). The main focus of the Tory study was on maritime tropical cyclogenesis, but it seems plausible to hypothesize that similar mechanisms would operate also over land, despite the larger surface stress and reduced local availability of surface moisture over land. In fact, Tory et al. (2007, p3202ff) described one case in which a low developed a little inland of the coast.

## The present study

The aim of the present study is to examine the intensification and structure of three lows that developed in January 2013 as seen in European Centre for Medium range Weather Forecasts (ECMWF) analyses. These analyses have a slightly higher effective horizontal resolution than TC-LAPS, albeit still not high enough to represent deep convection explicitly. The first low formed near the island of Timor and subsequently became tropical cyclone Narelle; the second formed about a week later a little further east, but did not attain cyclone strength; while the third developed over land before moving over the Gulf of Carpentaria and rapidly developing into tropical cyclone Oswald. The objective is to provide a vorticity perspective of these developments. Thermodynamic aspects of such developments will be presented elsewhere.

The paper is organized as follows. First, in section 'data sets' we present salient details of the data sets on which our analyses are based. In section 'vorticity and Okubo-Weiss diagnostics' we review the flux form of vorticity equation in pressure coordinates as well as the Okubo-Weiss diagnostic, which is useful for distinguishing regions where the vorticity is dominated by rotation flow as opposed to shear. In section 'features of the Australian monsoon in Jan 2013' we review briefly the mean structure of the Australian monsoon during January 2013. In sections 'genesis of tropical cyclone Narelle', 'an unnamed low over the Arafura sea' and 'tropical cyclone Oswald'

Figure 1 January mean fields at 850 mb: (a) Wind vectors and contours of zonal wind and geopotential height. Westerly wind component greater than  $5 \text{ m s}^{-1}$  shaded pink and greater than  $10 \text{ m s}^{-1}$  shaded red. Easterly winds greater than  $5 \text{ m s}^{-1}$  in magnitude shaded light blue. (b) Wind vectors, contours of geopotential height, and regions of elevated magnitudes of relative vorticity. Relative vorticity shading levels as shown on the label bar multiplied by  $10^{-5} \text{ s}^{-1}$ . Cyclonic values of vorticity are positive (red/pink shading), anticyclonic values are negative (light blue shading). Contour interval for geopotential height is 10 m in both panels. The lengths of the wind vectors are proportional to wind speed relative to the vector shown below each panel, which has a speed of  $15 \text{ m s}^{-1}$ .



we examine the genesis of the three lows referred to above. In section ‘synthesis’ we present a synthesis of the main results followed by a conclusions section.

## Data sets

The ECMWF analyses used for this study are available at the surface and at 25 pressure levels between 1000 mb and 1 mb. They cover the domain from  $100^\circ\text{E}$  to  $160^\circ\text{E}$ , from the Equator to  $30^\circ\text{S}$ , and have a horizontal grid spacing of 0.125 deg. The case studies are based largely on selected kinematic and thermodynamical fields extracted from these analyses supplemented by geostationary satellite imagery from the Japanese Meteorological Satellite (MTSAT). The analyses, which are obtained from a global four-dimensional variational analysis and prediction system (Bauer et al. 2011) are considered by forecasters to be as good as any available.

## Vorticity and Okubo-Weiss diagnostics

Considerable insight into the monsoon and the low pressure systems that form within it is provided by an analysis of the vorticity field and its time evolution. The vorticity tendency equation in pressure coordinates has a particularly concise form in which the local tendency can be written as the horizontal divergence of a horizontal flux (Haynes and McIntyre 1987; Raymond and Lopez-Carillo 2011; Tory et al. 2012; Raymond et al. 2014). Specifically, the equation for the local tendency of absolute vorticity  $\zeta_a$  may be written as

$$\frac{\partial \zeta_a}{\partial t} = -\nabla_h \cdot \mathbf{F}_{\zeta_a}, \quad (1)$$

where  $\mathbf{F}_{\zeta_a} = \mathbf{F}_{af} + \mathbf{F}_{naf}$ ,  $\mathbf{F}_{af} = \mathbf{u}_h \zeta_a$  and  $\mathbf{F}_{naf} = -\zeta_h \omega + \mathbf{k} \wedge \mathbf{F}_{fri}$ . Here  $\mathbf{u}_h$  is the horizontal velocity vector,  $\zeta_h$  is the approximate horizontal vorticity vector,  $\omega$  is the material derivative of pressure and plays the role of “vertical velocity” in pressure coordinates,  $\mathbf{F}_{fri}$  is the horizontal force per unit mass due to molecular effects and sub-grid-scale eddy momentum fluxes, and  $\mathbf{k}$  is a unit vector in the vertical.

The fact that the vorticity tendency can be written in the foregoing way implies, *inter alia*, that, in the absence of friction, the circulation about a fixed loop encircling a region of convection in the isobaric surface can change only by the *horizontal advection* of absolute vorticity into that loop, providing the loop is not intersected by orography (strictly this statement assumes that the vertical  $p$ -velocity vanishes on the loop). In convective regions there is both an advective flux ( $\mathbf{F}_{af}$ ) and a non-advective flux ( $\mathbf{F}_{naf}$ ). The non-advective flux is associated with vortex-tube-tilting processes as well as friction associated with sub-grid-scale eddy momentum transfer. The physics of

the non-advective fluxes is described elegantly by Raymond et al. (2014, their Figure 1)<sup>1</sup>. The foregoing formalism is mathematically equivalent to the material form of the equation for the vertical vorticity (e.g. Batchelor 1967; Holton 2004). The material form proves useful in understanding the *local amplification* of vorticity by deep convective updraughts, in contrast to the *concentration* of vorticity following from Eq. (1) within a fixed closed circuit (assuming of course that  $-\nabla_h \cdot \mathbf{F}_{\zeta_a} > 0$ ). It is only the concentration of vorticity that leads to an increase of circulation about a fixed circuit. The local amplification of vorticity does not, by itself, increase the circulation because the increase of vorticity by stretching is accompanied by a decrease in the area of the material vortex tube that is stretched with zero change of circulation about this material circuit. However, by mass continuity, stretching must be accompanied by flow convergence across the fixed circuit, which, if  $-\nabla_h \cdot \mathbf{F}_{\zeta_a} > 0$ , does lead to an increase in circulation about this circuit. Thus, the material form of the vorticity equation does not explicitly convey the area-integrated constraint contained by the flux form expressed by Eq. (1). In contrast, calculating the divergence of the advective flux does not distinguish between local changes in vorticity associated by pure advection and the generation of vorticity by stretching. One would need to calculate the stretching effect separately: see e.g. Raymond and Lopez-Carillo (2011, p156, column 2).

Although useful in characterizing local rotation, vertical vorticity may be associated with regions of strong horizontal shear deformation, which is detrimental to the formation of concentrated vortices. Favourable regions for vortex formation are those where the vorticity is dominated by pure rotation. Dunkerton et al. (2009) used depictions of the Okubo-Weiss (OW) parameter (defined here in the appendix) to highlight regions within the broadscale flow that tend to be most immune to horizontal shear deformation, i.e. regions where the flow is rotationally dominant. These are regions where convectively generated patches of vertical vorticity are most capable of congealing to form a monopole structure. We examine such diagnostics here also.

## Features of the Australian monsoon in January 2013

To set the scene we show in Fig. 1a the January-mean wind structure at 850 mb in the Australian region including the wind vectors and the contours of zonal wind component. Prominent features are the belt of relatively strong westerlies to the north of about 10°S with mostly weaker easterlies over a broad range of latitudes to the south. There are a few patches of stronger easterlies ( $> 5 \text{ m s}^{-1}$ ) primarily over the Australian continent. The region of westerlies is generally referred to as the monsoon flow, which is relatively deep, extending to approximately 500 mb (not shown), although the maximum wind speed is typically between 850 mb and 700 mb. The time-mean structure shown conceals much variability during the month as the band of peak westerlies progresses eastwards, tied to the phase of the Madden-Julian oscillation (MJO)<sup>2</sup>. The easterlies to the south exhibit variations in strength also as anticyclones progress eastwards to the south of the continent on the time scale of a week. The region sandwiched between the westerlies and the easterlies coincides with an elongated trough in the geopotential height. The trough line, indicated by the thick dashed line in Fig. 1a, arcs around the continent. These characteristics are broadly as described by McBride and Keenan (1982).

Figure 1b shows the corresponding field of January-mean relative vorticity at 850 mb, again with the wind vectors and geopotential height superimposed. As expected, there are patches of enhanced cyclonic vorticity broadly within the trough as well as a narrow zonal strip of cyclonic vorticity running along the northern side of the Indonesian archipelago with a less pronounced strip of anticyclonic vorticity on the southern side of the archipelago. Similar strips of cyclonic and anticyclonic vorticity are evident also along the island of New Guinea. These strips are presumably generated in the monsoonal flow by horizontal friction along the elevated terrain. The vorticity and geopotential patterns at 700 mb are similar, except that the anticyclonic component is barely evident along the archipelago and the extent of the cyclonic vorticity on the northern side is not so large (figure not shown). At 500 mb, these vorticity signatures have all but vanished (figure not shown). As in the wind fields, there is significant deviation in the vorticity pattern from the monthly mean pattern on a day-to-day basis, a feature that will be illustrated.

As strips of vorticity in a barotropic fluid can support Rossby edge waves and satisfy the necessary conditions for shear instability, they tend to be a breeding ground for coherent vortex structures (Ferreira and Schubert 1997 and references). Based on this idea, one could envisage that the strips of vorticity in the monsoon region have a similar tendency for generating nascent coherent vortices in the lower troposphere. If the kinematic and thermodynamic conditions are favourable, some of these coherent vortices may develop into low pressure disturbances or even tropical cyclones.

In the next three sections we examine the three tropical lows that developed during January 2013. The tracks and

<sup>1</sup>Raymond et al. use the form of the vorticity equation in height coordinates in which there is an additional baroclinic term, but this term is often small in the tropics.

<sup>2</sup>Data obtained from the Bureau of Meteorology's Madden-Julian oscillation monitoring website (<http://www.bom.gov.au/climate/mjo/>) showed the phase of the MJO to be on the border of Phases 3 and 4 on 1 January, and moving across the maritime continent region (Phases 4 and 5) by 10 January (see Wheeler and Hendon 2004 for a definition of these phases).

dates of these lows are shown in Fig. 2. The main focus of the paper will be on the formation of these lows and not on their subsequent intensification and/or demise.

Figure 2 (a) Tracks of the three tropical lows that formed during the January 2013 Australian monsoon season. The first and last of these lows developed into tropical cyclones Narelle and Oswald, while the second failed to achieve that status. Positions of the minimum geopotential at 850 mb indicated by cyclone symbols every 12 h. Positions at 0000 UTC shown by date.

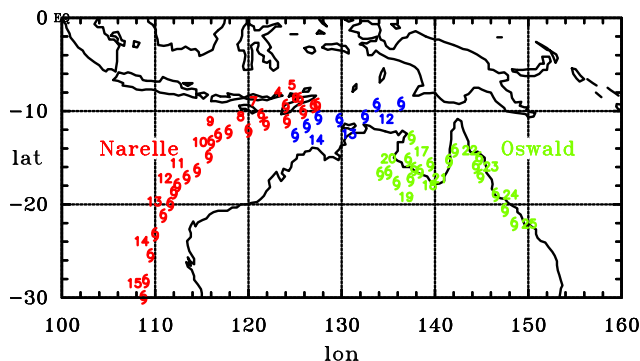
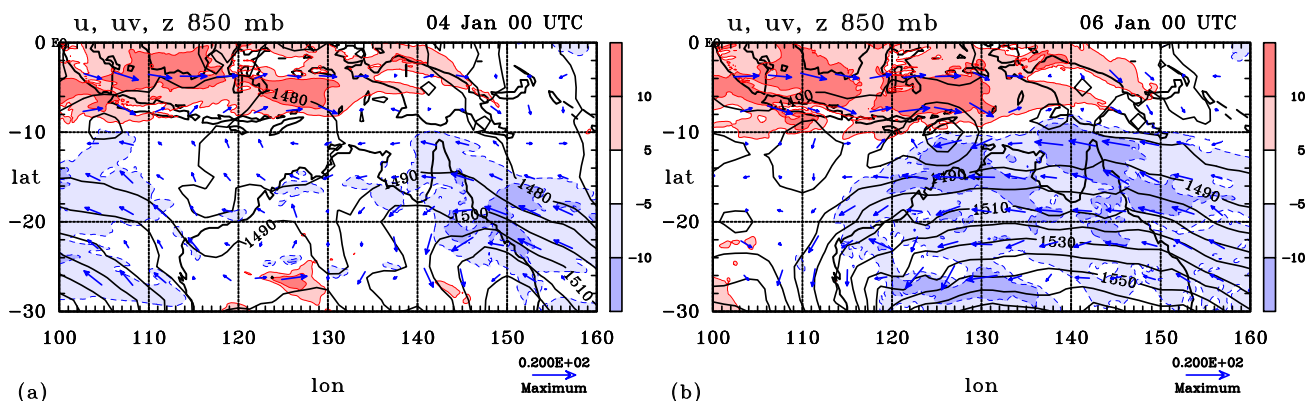


Figure 3 Wind vectors at 850 mb together with contours of the zonal wind component and geopotential height at 0000 UTC on (a) 4 January, and (b) 6 January 2013 illustrating the formation of the precursor low to tropical cyclone Narelle. Westerly wind component greater than  $5 \text{ m s}^{-1}$  shaded pink and greater than  $10 \text{ m s}^{-1}$  shaded red. Easterly winds greater than  $5 \text{ m s}^{-1}$  in magnitude shaded light blue, those greater than  $10 \text{ m s}^{-1}$  in magnitude shaded blue. Contour interval for geopotential height is 10 m. The lengths of the wind vectors are proportional to wind speed relative to the vector shown below each panel, which has a speed of  $20 \text{ m s}^{-1}$ .

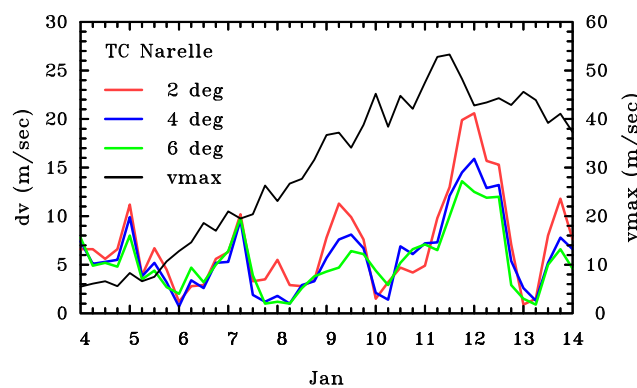


### Genesis of tropical cyclone Narelle

Figure 3 shows the wind structure at 850 mb together with the wind vectors and the contours of zonal wind component and geopotential height at 0000 UTC on 4 January and 6 January 2013, which should be compared with the January mean plot in Fig. 1a. On 4 January, four days prior to the naming of tropical cyclone Narelle, the strength of the monsoon westerlies is more variable than the mean and there is a region of locally strong westerlies to the north of Timor. There is a weak cyclonic gyre straddling Timor within a large area of low geopotential heights, but the easterly winds to the south of the island in the belt from  $120^{\circ}\text{E}$  to  $130^{\circ}\text{E}$  are relatively light. In the 48 h that followed, the changes in the large scale flow are dramatic with a major strengthening of the easterlies across Australia as an anticyclone moves eastwards to the south of the continent. In contrast, there is a small expansion in the area of the strong monsoon westerlies ( $> 10 \text{ m s}^{-1}$ ) in approximately the same longitude belt. Moreover, the circulation within the gyre has increased and there is an accompanying lowering of the 850 mb geopotential heights near the centre of the gyre.

The low continued to strengthen and was named tropical cyclone Narelle at 0600 UTC on 8 January. A time series of the minimum geopotential for tropical cyclone Narelle covering the period of interest here is shown later in Fig. 8a. Figure 4 shows the magnitude of the mean vertical wind shear<sup>3</sup> between 850 mb and 200 mb averaged over boxes  $2^\circ\text{lon} \times 2^\circ\text{lat}$ ,  $4^\circ\text{lon} \times 4^\circ\text{lat}$ , and  $6^\circ\text{lon} \times 6^\circ\text{lat}$  centred on the location of the minimum geopotential at 850 mb for TC Narelle together with the maximum wind speed at 850 mb within the  $2^\circ\text{lon} \times 2^\circ\text{lat}$  box. The latter serves as a measure of the vortex intensity<sup>4</sup>. Until about 1200 UTC on 11 January, the low was able to intensify in relatively weak shear ( $< 10 \text{ m s}^{-1}$ ), but then encountered a 36 h period of strong shear that led to a modest reduction in the intensity.

Figure 4 Mean vertical wind shear, characterized by the magnitude of the vector velocity difference between 850 mb and 200 mb, averaged over boxes  $2^\circ\text{lon} \times 2^\circ\text{lat}$ ,  $4^\circ\text{lon} \times 4^\circ\text{lat}$ , and  $6^\circ\text{lon} \times 6^\circ\text{lat}$  centred on the location of the minimum geopotential at 850 mb for TC Narelle and maximum wind speed at 850 mb within the  $2^\circ\text{lon} \times 2^\circ\text{lat}$  box.



A vorticity perspective of the foregoing development is illustrated in Fig. 5, which shows the corresponding fields of the vertical component of absolute vorticity together with the wind vectors and the contours of geopotential height at 850 mb. At 0000 UTC on 4 January, the most prominent feature in the absolute vorticity is the strip of elevated positive values between about  $5^\circ\text{S}$  and  $10^\circ\text{S}$  straddling the Indonesian archipelago with strong clumping at either end. The clump at the western edge of the strip has a pronounced recirculation associated with it as well as a weak isolated low in the geopotential height field. The one at the eastern end is colocated with the gyre near Timor referred to above, which was a little weaker than the western one at this time.

By 0000 UTC on 6 January, the clump of absolute vorticity near Timor has increased significantly in areal extent, the recirculating winds show a commensurate increase in strength and the geopotential has lowered further. In contrast, the nascent vortex to the west has weakened, but another one has formed just to the west of Papua New Guinea. These nascent vortices are quasi stationary and resemble the pouch-like circulations that have been described in the context of tropical cyclone formation over the Atlantic (Dunkerton et al. 2009). Over the Atlantic, the disturbances are normally translating in a horizontal shear flow and the recirculation is revealed when viewed in the co-moving frame.

Panel (c) of Fig. 5 shows the distribution of the OW parameter at the 850 mb level at the same time as the absolute vorticity shown in panel (b). At this time, the major feature of the OW-field in the monsoonal flow is the nascent vortex centred near Timor, while elsewhere in this flow positive OW-values are relatively small scale. This OW-feature is coherent up to 700 mb (not shown), and is one factor, at least, indicating that the vortex has the potential for further development. The need for the elevated OW values to be aligned vertically was found by Wang et al. (2012) and Tory et al. (2013) to be important in tropical cyclone formation. As shown in Fig. 4, there was almost no vertical shear at 0000 UTC on 6 January, a second factor favourable for development.

As a step towards understanding the role of deep convection in the spin up of low-level vorticity, we examine next areas of strong ( $> 0.5 \text{ Pa s}^{-1}$ ) vertical p-velocity ( $\omega$ ) at 500 mb (a proxy for deep convection in the ECMWF analysis) as the vortex evolves. These areas are shown in the left panels of Fig. 6 with the wind fields at 850 mb superimposed. The right panels of Fig. 6 show the corresponding fields of absolute vorticity at 850 mb with the advective flux vectors of absolute vorticity ( $\mathbf{F}_{af}$ ) superimposed.

<sup>3</sup>The shear is characterized here by the magnitude of the vector velocity difference between the two levels.

<sup>4</sup>At early times, before 1800 UTC on 6 January, the maximum wind speed in a  $4^\circ\text{lon} \times 4^\circ\text{lat}$  box is marginally larger, but as the low intensifies, the two maxima become essentially the same.

Figure 5 Wind vectors at 850 mb together with contours of the absolute vorticity (shaded) and geopotential height (thick blue contours) at 0000 UTC on (a) 4 January, and (b) 6 January 2013 illustrating the formation of the precursor low to tropical cyclone Narelle. Contour interval for geopotential height is 10 m. Absolute vorticity shading as shown on the label bar multiplied by  $10^{-3} \text{ s}^{-1}$ . Cyclonic values of vorticity are positive (red/pink shading), anticyclonic values are negative (light blue shading). (c) A similar plot but with contours of the Okubo-Weiss (OW) parameter (shaded) at 0000 UTC on 6 January. OW shading as shown on the label bar multiplied by  $10^{-8} \text{ s}^{-2}$ . Positive values have pink/red shading; negative values light blue shading. The lengths of the wind vectors are proportional to wind speed relative to the vector shown below each panel, which has a speed of  $20 \text{ m s}^{-1}$ .

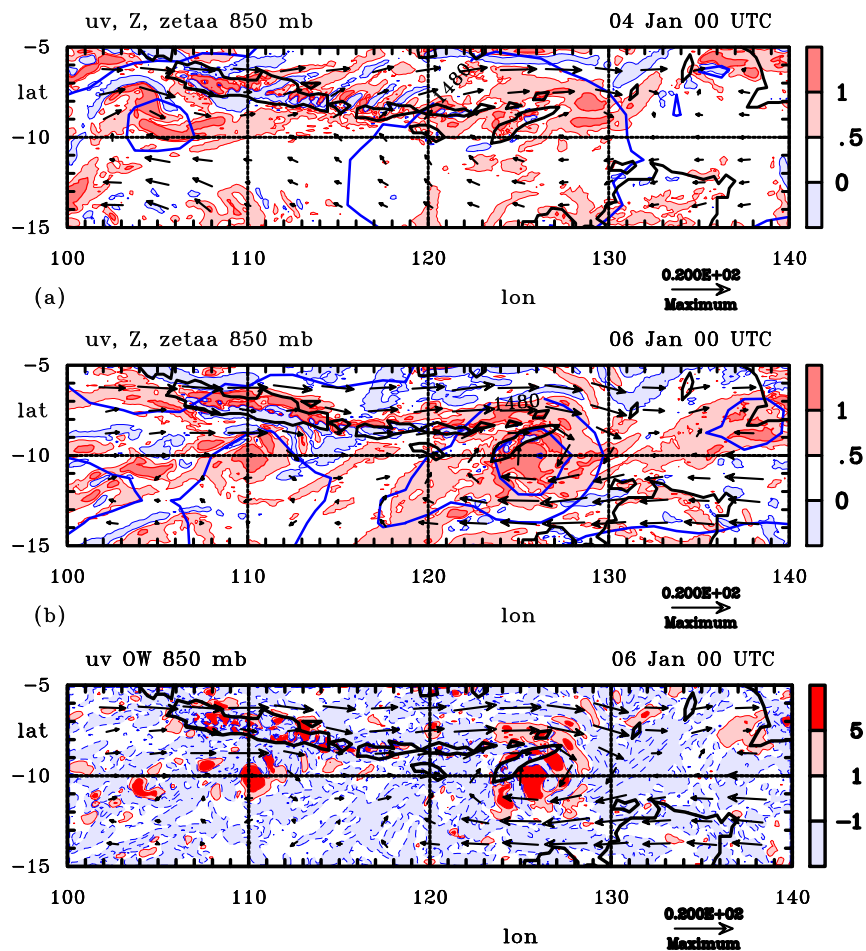
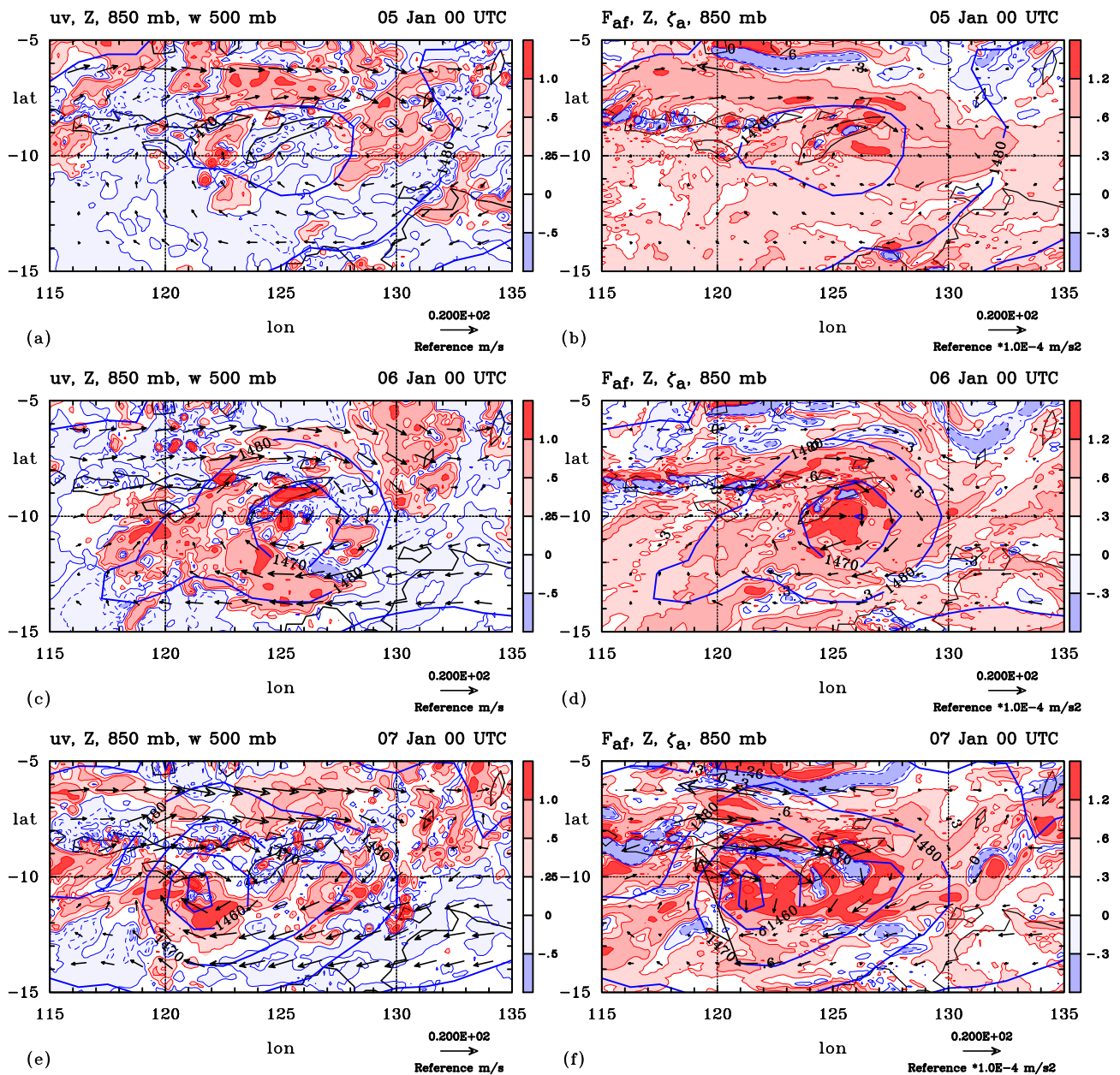


Figure 6 Wind vectors, contours of geopotential height together with contours of the vertical velocity at 500 mb (left panels) and vectors of the advective flux of absolute vorticity ( $F_{af}$ ) at 850 mb (right panels) at 0000 UTC on (a,b) 5 January, (c,d) 6 January, and (e,f) 7 January 2013, illustrating the formation of the precursor to tropical cyclone Narelle. Contour interval for geopotential height is 10 m. Vertical p-velocity ( $\omega$ ) shading as shown on the label bar in units  $\text{Pa s}^{-1}$ . Absolute vorticity shading as shown on the label bar multiplied by  $10^{-4} \text{ s}^{-1}$ . Upward vertical velocities (negative values of  $\omega$ ) and cyclonic values of absolute vorticity are plotted as positive (red/pink shading); negative values of vertical velocity (positive values of  $\omega$ ) and anticyclonic values of vorticity are plotted negative (light blue/blue shading). The lengths of the wind vectors are scaled with the 20  $\text{m s}^{-1}$  vector shown below each left panel. The lengths of the vorticity flux vectors are proportional to the vector shown below each right panel, which has a magnitude of  $2 \times 10^{-3} \text{ m s}^{-2}$ .





At 0000 UTC on 5 January we see significant areas of ascent in the monsoonal westerly flow to the north of the Indonesian archipelago and on the eastern and western sides of the broadscale circulation centred southeast of the island of Timor. These regions of ascent broadly overlap the primary regions of enhanced cyclonic absolute vorticity including the elongated region in the monsoonal flow as well as the regions to the west and east of the circulation centre. From a material perspective, this overlap is to be expected because ascent (or more precisely, the accompanying vertical gradient of the mass flux) implies that local absolute vorticity will be stretched. In the alternative view adopted in this paper, ascent implies low-level convergence, which, in turn, would imply a horizontal flux of absolute vorticity. The vectors  $\mathbf{F}_{af}$  shown indicate an advective flux of absolute vorticity around, and with a component towards, the centre of circulation of the nascent vortex.

By 0000 UTC on 6 January, the regions of strong ascent have reorganized and now form a band around the nascent vortex. Further, the cyclonic absolute vorticity has become wrapped up and consolidated around the developing vortex circulation. Again, there is a broad overlap in space of strong upward motion and elevated values of low-level cyclonic absolute vorticity. From the flux form of the vorticity equation, this upward motion leads to low-level convergence of absolute vorticity and therefore to an amplification of the tangential wind field of the nascent vortex about the centre of circulation. On the sub-vortex scale, there is a number of locally strong updraught cells in the analysis<sup>5</sup>, including one particularly intense cell near the centre of circulation as defined by the minimum of geopotential height at 850 mb. Presumably, these cells are contributing to the convergence of absolute vorticity and material stretching of vortex tubes, equivalent to the convergence of the advective flux in the flux form of the vorticity equation, Eq. (1). Recalling the material form of the vorticity equation, it follows that as a vortex tube is stretched by an updraught there will be a local amplification of both the vertical vorticity and horizontal wind speed.

As time proceeds, e.g. at 0000 UTC on 7 January, the low-level vorticity field has continued to amplify and deep convection proceeds to become more organized around the circulation centre. Again, a noteworthy feature is a strong cell of upward motion near the centre of the circulation. The evolution of the system-scale circulation about this centre will be discussed below.

Figure 7 Visible satellite imagery from the MTSAT geostationary satellite half an hour before 0000 UTC on (a) 5 January and (b) 6 January and contours of vertical motion ( $\omega$ ) at 500 mb from the ECMWF analyses at the 0000 UTC times. Contour interval: thin red contour  $0.25 \text{ Pa s}^{-1}$ , thick contours begin at  $0.5 \text{ Pa s}^{-1}$  and increase in intervals of  $0.5 \text{ Pa s}^{-1}$ . Red contours denote upward motion ( $\omega < 0$ ), blue contours subsidence.

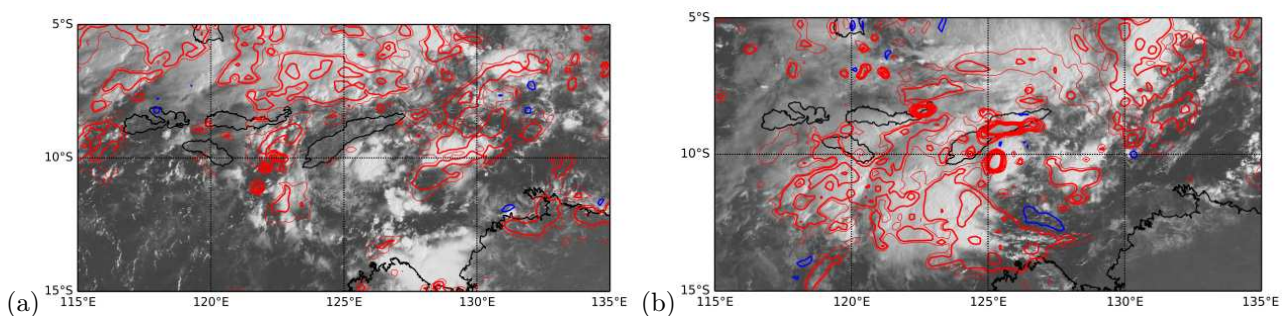


Figure 7 shows visible satellite imagery on the same horizontal domain as Fig. 6, but at 2330 UTC on 4 January and 5 January, half an hour earlier than the fields in panels (a) and (b) in Fig. 6. To ascertain the ability of the ECMWF analysis to capture the observed location of organized convective regions, the vertical motion from the analyses at 500 mb is superimposed on the satellite imagery. At 0000 UTC on 5 January, the analysis shows several analysed convective systems to the north and east of Timor, most of them overlapping or close to observed systems, but with the exception of an observed system centred just southeast of Timor and the cloud complex seen over the Bonaparte Gulf. Moreover, the analysis has ascent over the coastal fringe of the “Top End”, which is not observed. The comparison at 0000 UTC on 6 January has improved noticeably, in part as the nascent vortex near Timor becomes more organized. In particular, the banded cloud structures wrapping around the circulation centre in the visible imagery are captured qualitatively well by the analysis. Comparisons between the locations of moderate ascent in the analysis and clouds in the visible imagery at other times (not shown) convey essentially a similar picture. The foregoing comparisons give confidence that the analyses have adequate skill in reproducing the broadscale convective features that are observed.

<sup>5</sup>Of course, the cells in the analysis do not represent individual observed updraughts. The ECMWF forecast and analysis system uses a convective parameterization scheme.

Figure 8 shows time-height cross sections of various quantities averaged over a square box  $2^\circ\text{lon} \times 2^\circ\text{lat}$  centred on the minimum geopotential at 850 mb. These quantities include the vertical mass flux (approximated here by  $-\omega/g$ ), the temperature, the relative humidity, and the pseudo-equivalent potential temperature,  $\theta_e$ . Shown also is a time-height cross section of the circulation around the box and a time series of the minimum geopotential at 850 mb for the same 6 day period. Notable features of the vertical mass flux are the two “bursts” centred at 1800 UTC on 6 and 7 January followed by a sustained period of strong ascent from 0600 UTC on 8 January (Fig. 8c). Interestingly, the two bursts coincide with the observed time of the convective maximum over the ocean, indicative of some skill of the ECMWF forecast and analysis system in capturing the diurnal cycle of deep convection. Moreover, they are each accompanied by a slight deepening of the low (Fig. 8a). The onset of sustained ascent was followed by an accelerated period of deepening and occurred about the time that the system was named.

Early in the evolution of the low, up to 1200 UTC on 5 January, the circulation was a maximum at a pressure level of about 600 mb, but this maximum moved down to about 850 mb as the low intensified (Fig. 8e). The relative humidity averaged over the square box was generally high in the low to middle troposphere as the low developed (Fig. 8d) and the temperature increased, first at upper levels, the increase progressively descending to the surface (Fig. 8b). However, there were periods until about 0600 UTC on 8 January of slightly reduced temperature, mostly below 800 mb and mostly less than  $0.5^\circ\text{C}$  in magnitude. These were presumably associated with convectively-induced mesoscale downdraughts. The time-height cross-sections of  $\theta_e$  (Fig. 8f) corroborates the effects of the moistening of the middle troposphere as the low intensified.

## An unnamed low over the Arafura sea

Less than a week after the formation of Narelle, a second low formed in the Arafura sea, but further to the east. Although this low did not ultimately reach tropical cyclone strength, it is scientifically interesting in the context of low formation in the monsoon regime.

Figure 9 shows the wind vectors and geopotential height contours at 850 mb on selected days during the formation of the low. Regions of zonal flow exceeding 5 and  $10 \text{ m s}^{-1}$  are highlighted also. Although the most prominent feature is still tropical cyclone Narelle, our focus is on the monsoonal flow as it impinges on the island of Papua New Guinea. Close inspection of the wind vectors at 0000 UTC 10 January reveals a splitting of the monsoonal flow to the northeast of the top end of Australia, with one branch entering the circulation of Narelle from the northeast, and the other flowing eastwards towards New Guinea. The latter flow branch appears to be deflected by the high terrain of New Guinea and flows southwards towards Cape York Peninsula. By 0000 UTC 11 January the flow near the Cape has turned towards the southwest and there is evidence of a strengthening circulation in this region. One day later at 0000 UTC 12 January, there is a clear recirculating flow to the north of the top end, marked by a closed low in geopotential height. The winds about the low have strengthened relative to their magnitude on the previous day. Two days later, the low has moved slowly west-southwestwards and has strengthened a little more.

Figure 10 shows the magnitude of the mean vertical wind shear between 850 mb and 200 mb averaged over boxes  $2^\circ\text{lon} \times 2^\circ\text{lat}$ ,  $4^\circ\text{lon} \times 4^\circ\text{lat}$ , and  $6^\circ\text{lon} \times 6^\circ\text{lat}$  centred on the location of the minimum geopotential at 850 mb for the low, together with the maximum wind speed at 850 mb within the  $2^\circ\text{lon} \times 2^\circ\text{lat}$  box (a time series of the minimum geopotential height at 850 mb is shown later in Fig. 14a). While the low was intensifying slowly until 1800 UTC 14 January, it was battling against moderate shear from about 0600 UTC on 13 January. The shear then increased to more than  $20 \text{ m s}^{-1}$ , which apparently contributed to a significant reduction of intensity of the low.

As in the examination of the low-level spin up of Narelle, we show in Fig. 11 areas of strong  $\omega$  (magnitude  $> 0.5 \text{ Pa s}^{-1}$ ) at 500 mb together with regions of enhanced 850 mb absolute vorticity. At 0000 UTC on 11 January, there is a number of regions of deep convection, both in the monsoonal flow and in the nascent circulation to the northeast of the top end. In the same general area there are numerous patches of enhanced absolute vorticity that appear to be undergoing some differential elongation as the patches flow around the nascent centre of circulation.

After one and a half days at 1200 UTC on 12 January, the strong upward motion is distributed approximately in a ring within the broad-scale circulation, and there are a few regions of intense updraughts embedded within these convective areas. The absolute vorticity forms a similar ring that is approximately coincident with the strong convection. The horizontal scale of the nascent circulation is large, spanning approximately eight degrees of latitude in diameter. The circulation has an annular character and there are two nearly contiguous regions of subsidence near its centre.

Figure 12 shows infrared satellite imagery at 1130 UTC on 11 January on the same horizontal domain as Fig. 11, half an hour earlier than the corresponding vertical velocity and geopotential height fields. Again, as a further test of the integrity of the analysis to represent the general areas of deep convection, the vertical motion from the analyses at 500 mb are superimposed on the infrared imagery at this time (local night-time). The analysis captures reasonably well the convective features around the aforementioned ring-like circulation of the low. The

Figure 8 (a) Time series of minimum geopotential at 850 mb for the low that became tropical cyclone Narelle. Time-height cross sections of system averaged quantities within a box  $2^\circ\text{lon} \times 2^\circ\text{lat}$ , centred on the location of the minimum geopotential at 850 mb. These include (b) the temperature deviation from that at the start of the time series, (c) vertical mass flux (units  $\text{kg m}^{-2} \text{s}^{-1}$ ), (d) the relative humidity (in per cent), and (f) pseudo-equivalent potential temperature (in K). Panel (e) shows the normalized circulation around the box (units  $\text{m s}^{-1}$ ).

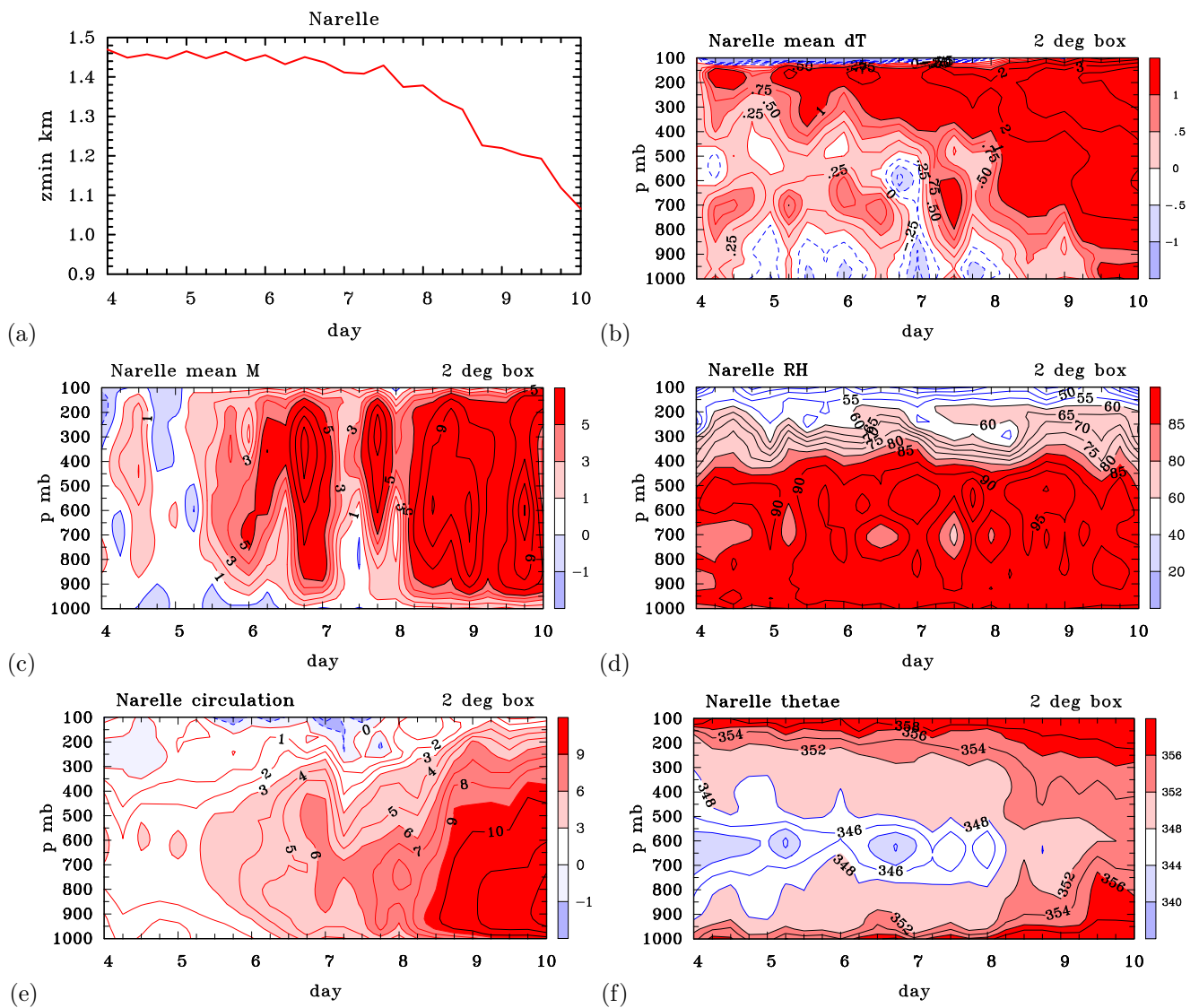


Figure 9 Wind vectors at 850 mb together with contours of the zonal wind component and geopotential height at 0000 UTC on (a) 10 January, (b) 11 January, (c) 12 January, and (d) 14 January 2013, illustrating the formation of the unnamed low that followed tropical cyclone Narelle. Westerly wind component greater than  $5 \text{ m s}^{-1}$  shaded pink, that greater than  $10 \text{ m s}^{-1}$  shaded red. Easterly winds greater than  $5 \text{ m s}^{-1}$  in magnitude shaded light blue, those greater than  $10 \text{ m s}^{-1}$  in magnitude shaded blue. Contour interval for geopotential height is  $10 \text{ m}$ . The lengths of the wind vectors are proportional to wind speed relative to the vector shown below each panel, which has a speed of  $20 \text{ m s}^{-1}$ .

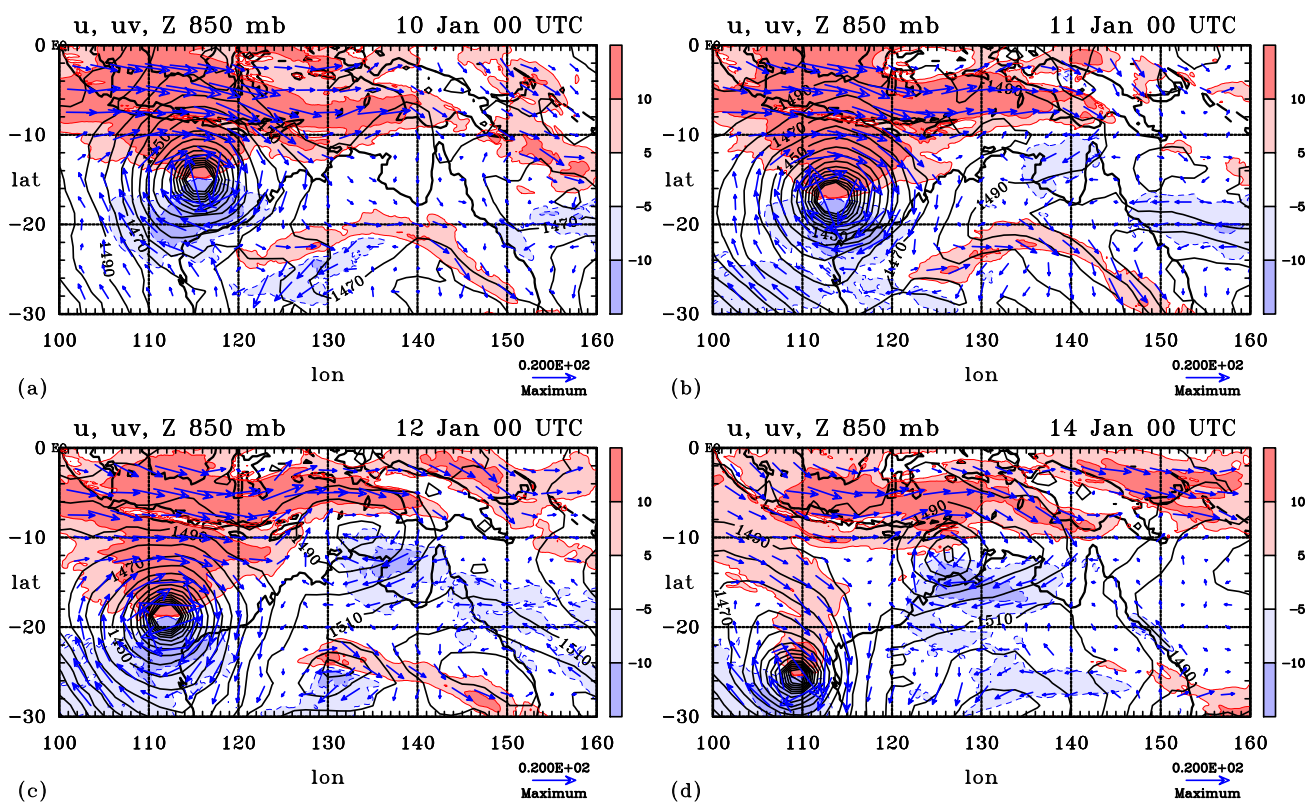


Figure 10 Mean vertical wind shear, characterized by the magnitude of the vector velocity difference between 850 mb and 200 mb, averaged over boxes  $2^\circ\text{lon} \times 2^\circ\text{lat}$ ,  $4^\circ\text{lon} \times 4^\circ\text{lat}$ , and  $6^\circ\text{lon} \times 6^\circ\text{lat}$  centred on the location of the minimum geopotential at 850 mb for the unnamed low that followed TC Narelle and maximum wind speed at 850 mb within the  $2^\circ\text{lon} \times 2^\circ\text{lat}$  box.

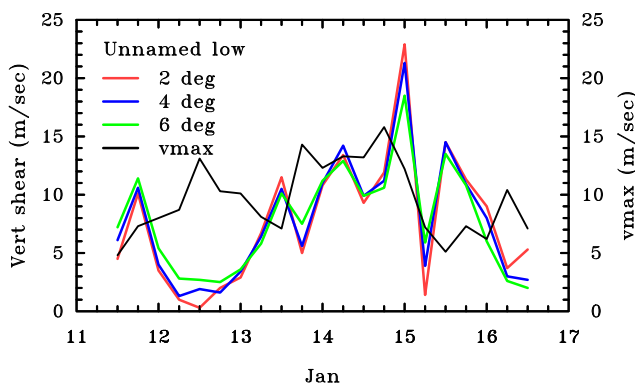
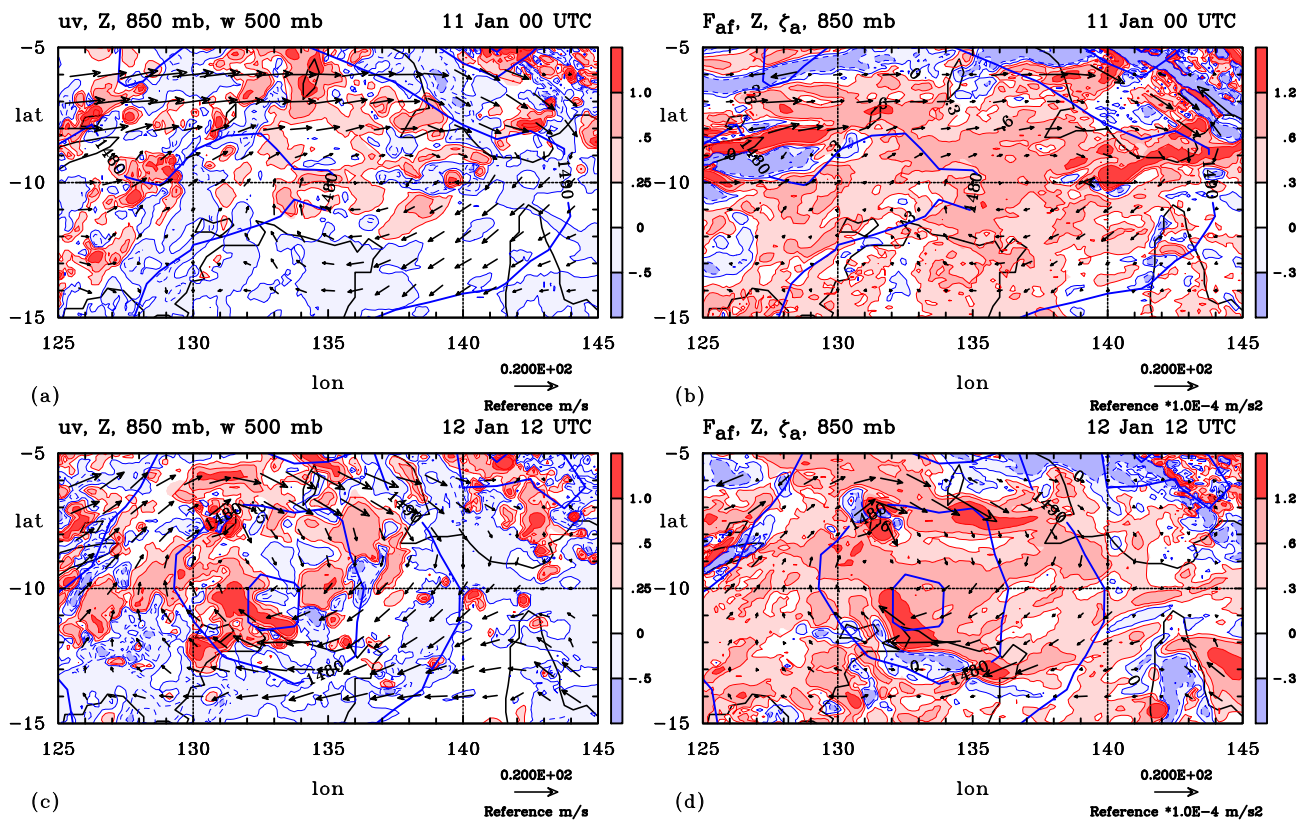


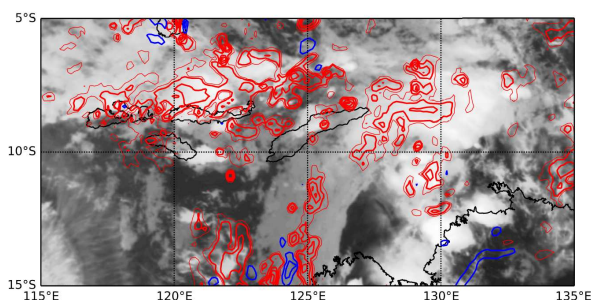
Figure 11 Wind vectors, contours of geopotential height together with contours of the vertical p-velocity ( $\omega$ ) at 500 mb (left panels) and contours of the advective flux of absolute vorticity ( $F_{af}$ ) at 850 mb (right panels) at 0000 UTC on (a,b) at 0000 UTC on 11 January, and (c,d) 1200 UTC on 12 January 2013, illustrating the formation of the unnamed low that followed tropical cyclone Narelle. Contour interval for geopotential height is 10 m. Vertical p-velocity shading as shown on the label bar in units  $\text{Pa s}^{-1}$ . Absolute vorticity shading as shown on the label bar multiplied by  $10^{-4} \text{ s}^{-1}$ . Upward vertical velocities (negative values of  $\omega$ ) and cyclonic values of absolute vorticity are plotted as positive (red/pink shading); negative values of vertical velocity (positive values of  $\omega$ ) and anticyclonic values of vorticity are plotted negative (light blue/blue shading). The lengths of the wind vectors are scaled with the  $20 \text{ m s}^{-1}$  vector shown below each left panel. The lengths of the vorticity flux vectors are proportional to the vector shown below each right panel, which has a magnitude of  $2 \times 10^{-4} \text{ m s}^{-2}$ .



convective activity along the Indonesian archipelago is broadly captured also.

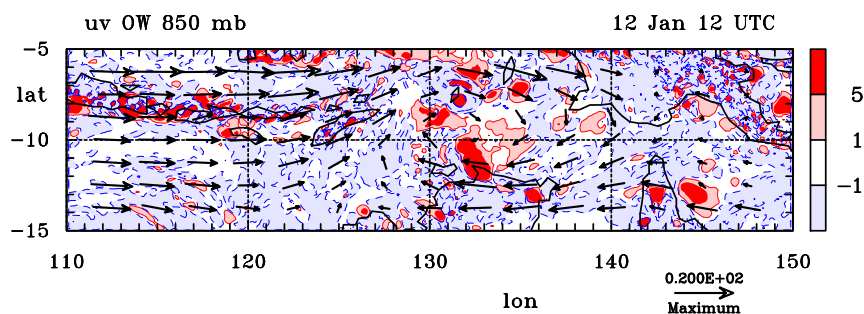
Figure 13 shows the distribution of the OW parameter at the 850 mb level at the same time as the absolute vorticity shown in panel (d) in Fig. 11. While the major feature is the coherent region of positive OW-values near the circulation centre (approx 9°S, 132°E), the largest values in this region lie more than 1 deg. from this centre, unlike the situation for Narelle shown in Fig. 5c.

Figure 12 Infrared ( 10.5 – 11.5  $\mu\text{m}$ ) satellite imagery from the MTSAT geostationary satellite at 1130 UTC on 11 January. Contours of vertical motion at 500 mb from the ECMWF analyses half an hour later are overlain. Contour interval: thin red contour 0.25 Pa s<sup>-1</sup>, thick contours begin at 0.5 Pa s<sup>-1</sup> and increase in intervals of 0.5 Pa s<sup>-1</sup>. Red contours for ascent, blue contours for descent.



Comparing the time series of minimum geopotential for this low (Fig. 14a) with that for Narelle (Fig. 8a) indicates the degree to which the low was struggling in a hostile environment. This picture is reinforced by examining time-height cross sections of system averaged quantities within or around a box 2° lon × 2° lat, centred on the location of the minimum geopotential at 850 mb for the unnamed low. These are shown also in Fig. 14 and include the vertical mass flux, the normalized circulation around the box, and the relative humidity. Consistent with the horizontal cross sections in Fig. 11, although the low contained bursts of deep convection in its early stages, this convection never consolidated near the centre of circulation (Fig. 14b) and the circulation about the 2° lon × 2° lat box never became strong compared with its behaviour in Narelle (compare Fig. 14c with Fig. 8c). Invoking the conventional mechanism for spin up (see e.g. Montgomery and Smith 2014), deep convection near the centre of circulation would be required to converge absolute vorticity needed for the spin up of the inner-core. Inspection of Fig. 14d shows that strong drying of the middle troposphere in the inner core occurs simultaneously with the onset of strong vertical shear (see Fig. 10). This drying would have suppressed deep convection in that region, thereby reducing the ability of the system to concentrate vorticity (Kilroy and Smith 2013) and increase its circulation (see section 3).

Figure 13 Wind vectors at 850 mb together with contours of the Okubo-Weiss (OW) parameter (shaded) at 0000 UTC on 1200 UTC on 12 January illustrating the formation of the unnamed low. OW shading as shown on the label bar multiplied by 10<sup>-8</sup> s<sup>-2</sup>. Positive values have pink/red shading; negative values light blue shading. The lengths of the wind vectors are proportional to wind speed relative to the vector shown below the figure, which has a speed of 20 m s<sup>-1</sup>.



## Tropical cyclone Oswald

On 17 January, an area of low pressure developed over the Gulf of Carpentaria. This low pressure area was situated within a region of low wind shear and high sea surface temperatures, conditions generally believed to be favourable for low development. The following day, the system was monitored as a tropical low by the Darwin Tropical Cyclone Warning System. The storm made landfall southwest of Borroloola early on 19 January. Over the next two days, the system completed a clockwise loop before re-emerging into the Gulf of Carpentaria, and being over water, it quickly organized and strengthened into a tropical cyclone early on 21 January. The storm crossed Cape York Peninsula attaining recorded winds of  $65 \text{ km h}^{-1}$  ( $18 \text{ m s}^{-1}$ ) and then moved southwards along the eastern coastline, producing torrential rains over much of Queensland.

To investigate the formation and evolution of this low, we begin by showing in Fig. 15 a sequence of 850 mb wind analyses similar to those in Figs. 3 and 9. Here the period presented is the time interval spanning 0000 UTC 16 January to 0000 UTC 20 January during the evolution of the precursor disturbance to Tropical Cyclone Oswald. The monsoonal flow at 0000 UTC on 16 January is similar to that on 10 January with strong westerlies being deflected to northerlies over Cape York Peninsula (compare Figs. 15a with 9a). The main difference is the existence of a low in the middle troposphere of middle-latitude origin to the south of the gulf on 16 January. This low is associated with a mid-level potential vorticity anomaly that became detached from a strip of potential vorticity within a large-amplitude trough along the east coast of Australia (M. Reeder, personal communication). The low-level centre moved subsequently westwards and, by 0000 UTC 17 January, a second centre had formed over the gulf (Fig. 15b). However, the 500 mb low remained as a coherent feature over the developing system (not shown). By 0000 UTC on 18 January, the low over the gulf had strengthened and its centre was about to move over land. During the next 48 h, this low tracked westwards and strengthened further (Fig. 15d). Subsequently, the system tracked east-northeastwards over the gulf where it intensified to become tropical cyclone Oswald (not shown). Note that this low was part of a continental scale low that incorporated the monsoonal flow itself.

Figure 16 shows the mean vertical wind shear averaged over boxes  $2^\circ\text{lat}\times 2^\circ\text{lon}$ ,  $4^\circ\text{lat}\times 4^\circ\text{lon}$ , and  $6^\circ\text{lat}\times 6^\circ\text{lon}$  centred on the location of the minimum geopotential at 850 mb for the Tropical Cyclone Oswald, together with the maximum wind speed at 850 mb within the  $2^\circ\text{lat}\times 2^\circ\text{lon}$  box. Based on this wind speed, the low began to intensify late on 17 January while it was over the gulf. The intensification continued as the low performed a loop over land and became rapid as the system tracked again over the gulf on 22 January. The intensification was soon arrested as the low made landfall over Cape York Peninsula on 23 January. However, the whole period of evolution took place in conditions of relatively weak vertical shear.

Similar to Figs. 6 and 11, Fig. 17 shows the vertical velocity distribution at 500 mb with the 850 mb wind vectors and the absolute vorticity at 850 mb together with the advective flux vectors  $\mathbf{F}_{\text{af}}$ . At 0000 UTC 17 January, there is deep convection around the top end associated with the monsoonal flow and there is a band also of deep convection on the southwestern side of the developing low. Filaments of cyclonic absolute vorticity are curving around the Top End in the monsoonal flow and feeding into the gulf, while there is a broad patch of enhanced cyclonic vorticity coincident with the low.

At 0000 UTC 18 January there is strong ascent over the southeastern part of the gulf and in a band over the southern part of Cape York Peninsula. One day later, convection in most of the low has all but ceased, but the absolute vorticity has both consolidated and intensified relative to the previous day (not shown). Much of this vorticity was concentrated by the aggregate of prior convective cycles. One day later, at 0000 UTC on 20 January, intense cells of deep convection are apparent near the vortex center and the vortex has intensified a little further. Also noteworthy is the elliptical pattern of geopotential, which is reflected in the elongated pattern of cyclonic absolute vorticity in the direction of the major axis of the ellipse.

Figure 18 shows the distribution of the OW parameter at 850 mb at 0000 UTC on 18 January when the low was about to cross over the land. At this time, there is a broad region of positive OW over much of the gulf with a significant patch of enhanced OW marking the low in the southern gulf. These elevated OW values remained as the low tracked westwards over land (not shown).

Figure 19 shows the satellite imagery at 2330 UTC on 18 January and 20 January with contours of vertical motion at 500 mb from the analyses superimposed. As in the other examples shown (cf. Figs. 7 and 13), the analyses have reasonable skill in broadly locating areas of deep convection where they are observed, but as might be expected, there are some localized areas where the agreement is poor.

Similar to Figs. 8 and 14, Fig. 20 shows time-height cross sections of vertical mass flux and pseudo-equivalent potential temperature averaged over a square box  $2^\circ\text{lon}\times 2^\circ\text{lat}$  centred on the minimum geopotential at 850 mb. The figure shows also a time series of the minimum geopotential at 850 mb and a time-height cross section of the circulation around the box. The time period covers the early period while the low was over the gulf and the period of slow intensification while it was over land. As in the case of Narelle (cf. Fig. 8), there were bursts of convective activity near the centre of circulation, which by 20 January had become more persistent (Fig. 20b). The

Figure 14 (a) Time series of minimum geopotential at 850 mb for the unnamed low that followed tropical cyclone Narelle. (b) Time-height cross-section of system averaged quantities within (or in the case of (c) around) a box  $2^\circ\text{lon} \times 2^\circ\text{lat}$ , centred on the location of the minimum geopotential at 850 mb. These include (b) the vertical mass flux per unit area (units  $\text{kg m}^{-2} \text{s}^{-1}$ ), (c) the normalized circulation around the box (units  $\text{m s}^{-1}$ ), and (d) the relative humidity.

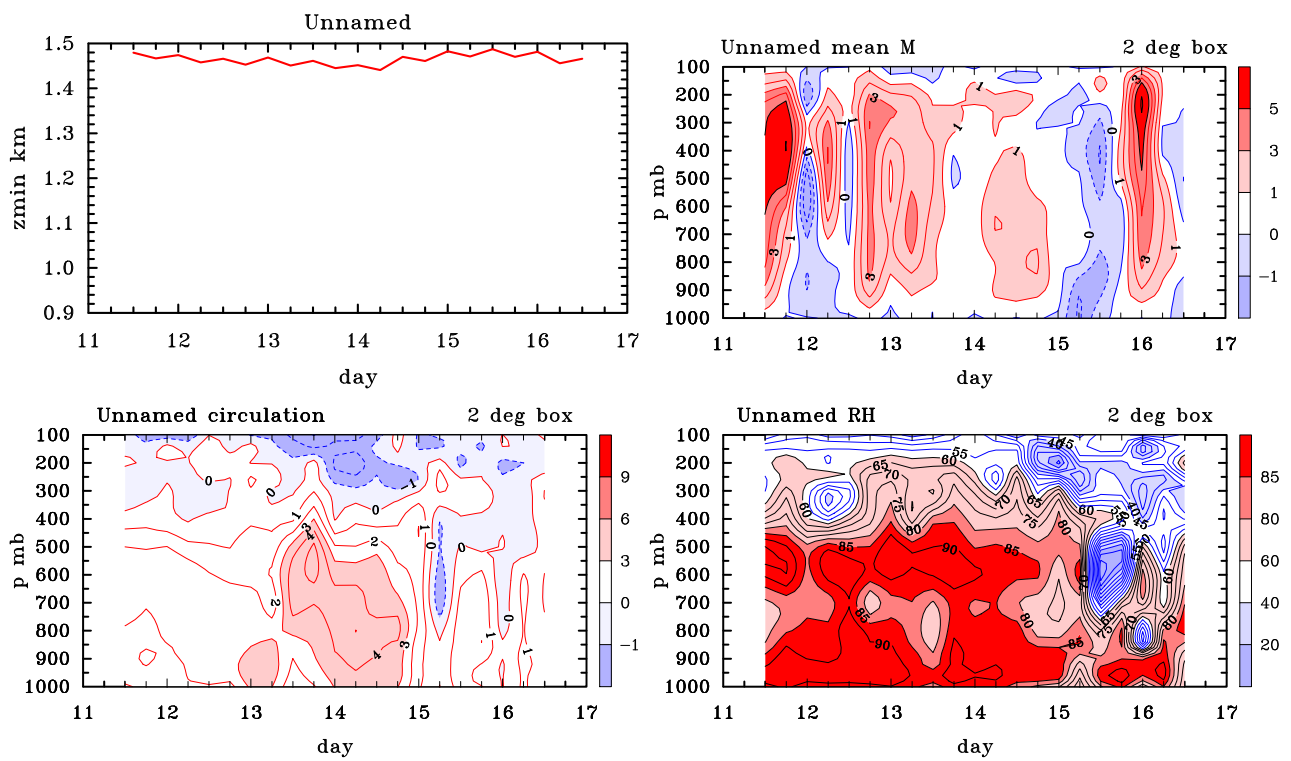
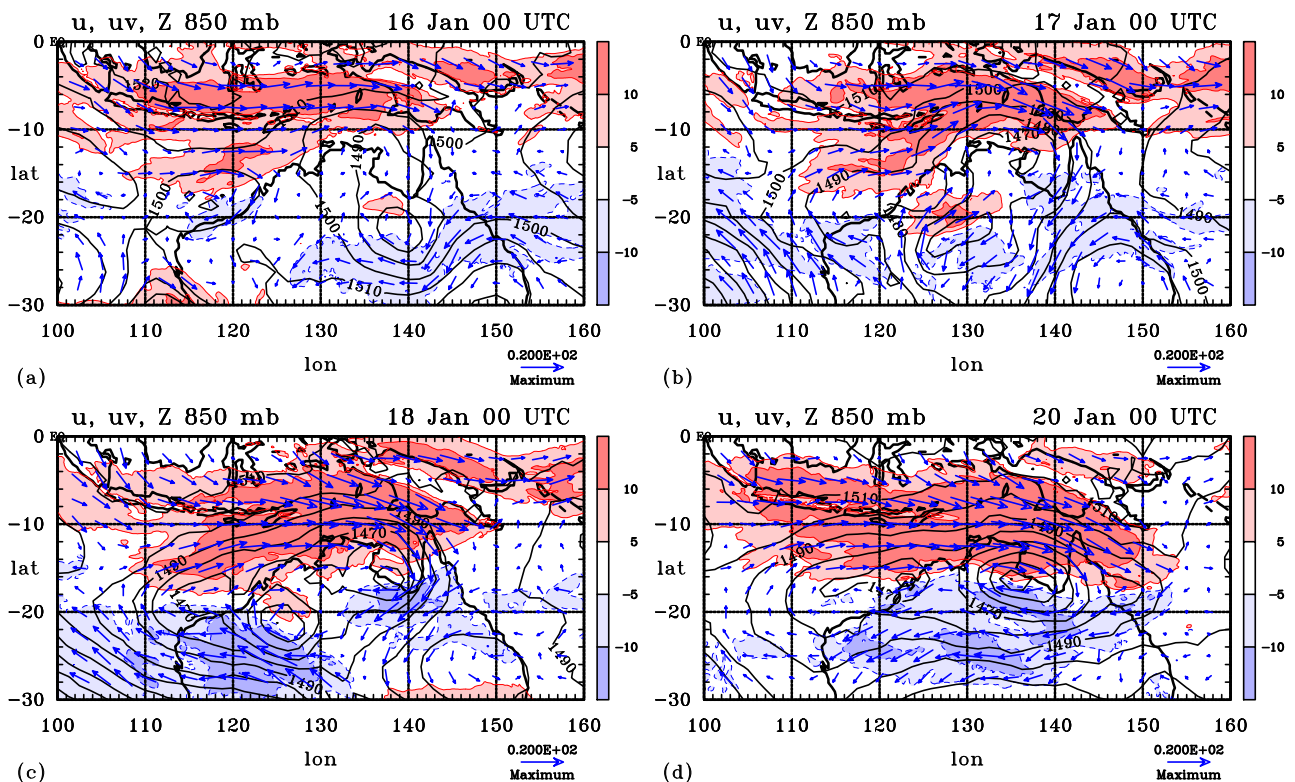


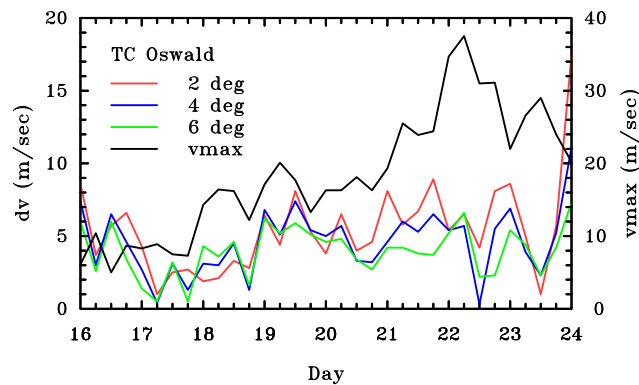


Figure 15 Wind vectors at 850 mb together with contours of the zonal wind component and geopotential height at 0000 UTC on (a) 16 January, (b) 17 January, (c) 18 January, and (d) 20 January 2013 illustrating the formation of the low that ultimately became tropical cyclone Oswald. Westerly wind component greater than  $5 \text{ m s}^{-1}$  shaded pink, that greater than  $10 \text{ m s}^{-1}$  shaded red. Easterly winds greater than  $5 \text{ m s}^{-1}$  in magnitude shaded light blue, those greater than  $10 \text{ m s}^{-1}$  in magnitude shaded blue. Contour interval for geopotential height is 10 m. The lengths of the wind vectors are scaled with the  $20 \text{ m s}^{-1}$  vector shown below each left panel. The lengths of the vorticity flux vectors are proportional to the vector shown below each right panel, which has a magnitude of  $2 \times 10^{-3} \text{ m s}^{-2}$ .



circulation increased steadily during the period shown and was a maximum in the lower troposphere at all times shown: this was clearly a “bottom up” development (Fig. 20c). As in the Narelle case also, there was a progressive moistening of the middle troposphere as evidenced in the weakening of the middle tropospheric minimum in  $\theta_e$  (Fig. 20d).

Figure 16 Mean vertical wind shear averaged over boxes  $2^\circ\text{lat} \times 2^\circ\text{lon}$  centred on the location of the minimum geopotential at 850 mb for TC Oswald.



## Synthesis

The ECMWF analyses of the January 2013 monsoon described herein provide a vorticity perspective of the monsoon itself and of vortex formation within it. Averaged over the month, the monsoon is characterized by a strip of enhanced low-level cyclonic vertical vorticity along the Indonesian archipelago marking the Inter Tropical Convergence Zone (ITCZ) with additional strips marking the monsoon shear line. At any one time, the vorticity field has considerable fine-scale structure on account of the local generation of vorticity by deep convection. Furthermore, its structure can deviate significantly from the monthly average. On the scale of the monsoon flow (typically several thousand kilometres), the vorticity distribution in an isobaric surface has to be largely the result of the convectively-induced import of planetary vorticity into the monsoon region. This statement follows from a powerful theorem of Haynes and McIntyre (1987) showing that there can be no net generation of absolute vorticity in an isobaric surface averaged over the globe and that there is no net vertical transport of vertical vorticity into this surface.

Areas of deep convection developing within the “sea” of mostly cyclonic absolute vorticity act as focal points to produce further concentrations of vorticity, primarily in association with the divergence of the advective vorticity flux, leading to the formation of a large-scale monsoonal gyre. These gyres are accompanied by extensive areas of gale-force winds and have low surface pressure. A succession of such gyres may form during the monsoon season. The development of these gyres is akin to the roll up of vorticity in easterly waves described by Dunkerton et al. (2009). In analogy with the situation within easterly waves, these gyres act as protected “pouches” in which the low at the centre of the gyre can intensify further.

The ECMWF analyses suggest that intensification of the low requires periodic bursts of deep convection near the centre of the gyre to promote the further concentration of cyclonic vorticity near the centre. As discussed in section ‘vorticity and Okubo-Weiss diagnostics’, this concentration of vorticity increases the local circulation about the centre, which amounts to increasing the local tangential wind speed.

Bursts of deep convection near the centre of circulation would be aided by frictional convergence of moisture laden air towards the centre of the gyre (see e.g. Montgomery and Smith 2014, Fig. 4). The associated ascent within the boundary layer near the centre would weaken the local convective inhibition there and assist air parcels in reaching their level of free convection. Since water temperatures in the region are high (around  $30^\circ\text{C}$ ), the main impediment to the further intensification of the low would appear to be excessive vertical wind shear near the circulation centre. The vortices in the analyses presented here are able to amplify in wind shears below about  $10 \text{ m s}^{-1}$ .

In some cases the centre of the monsoon gyre may form over land. Both observations and the ECMWF analyses indicate that moisture levels are high enough in the monsoon circulation to enable lows to intensify over land by essentially the same mechanism, i.e. the convectively-induced concentration of absolute vorticity by periodic bursts of convection near the circulation centre. Again the main requirement seems to be that levels of vertical shear over the vortex core region do not become excessive.

Figure 17 Wind vectors, contours of geopotential height together with contours of the vertical p-velocity ( $\omega$ ) at 500 mb (left panels) and contours of the advective flux of absolute vorticity ( $F_{af}$ ) at 850 mb (right panels) at 0000 UTC on (a,b) at 0000 UTC on 17 January, (c,d) on 18 January, and (e,f) 20 January 2013, illustrating the formation of the precursor to tropical cyclone Oswald. Contour interval for geopotential height is 10 m. Vertical p-velocity shading as shown on the label bar in units  $\text{Pa s}^{-1}$ . Absolute vorticity shading as shown on the label bar multiplied by  $10^{-4} \text{ s}^{-1}$ . Upward vertical velocities (negative values of  $\omega$ ) and cyclonic values of absolute vorticity are plotted as positive (red/pink shading); negative values of vertical velocity (positive values of  $\omega$ ) and anticyclonic values of vorticity are plotted negative (light blue/blue shading). The lengths of the wind vectors are scaled with the  $20 \text{ m s}^{-1}$  vector shown below each left panel. The lengths of the vorticity flux vectors are proportional to the vector shown below each right panel, which has a magnitude of  $2 \times 10^{-3} \text{ m s}^{-2}$ .

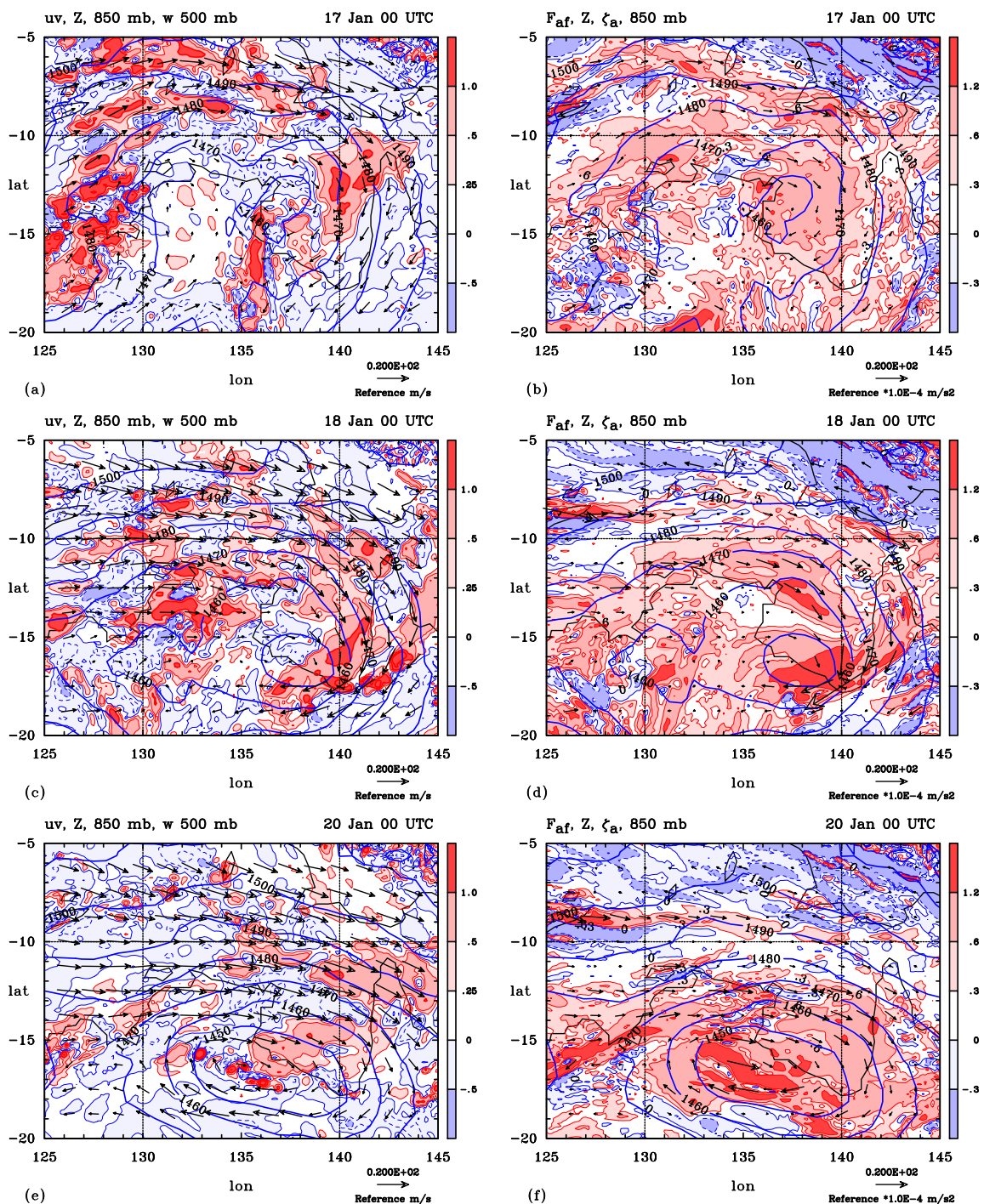


Figure 18 Wind vectors at 850 mb together with contours of the Okubo-Weiss (OW) parameter (shaded) at 0000 UTC on 18 January 2013 during the formation of the precursor to tropical cyclone Oswald. OW shading as shown on the label bar multiplied by  $10^{-8} \text{ s}^{-2}$ . Positive values have pink/red shading; negative values light blue shading.

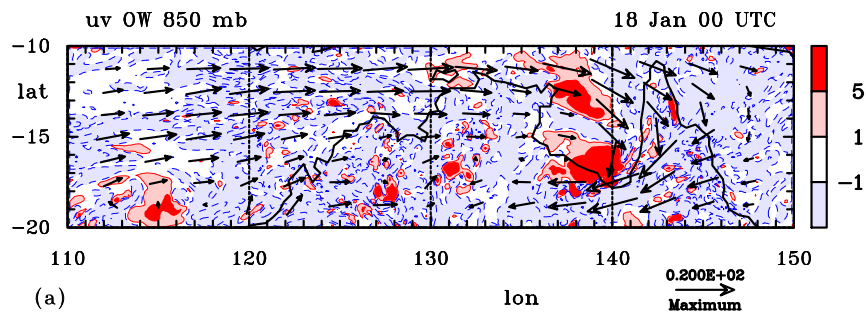


Figure 19 Visible satellite imagery from the MTSAT geostationary satellite at 2330 UTC on (a) 17 January and (b) 19 January. Contours of vertical motion at 500 mb from the ECMWF analyses half an hour later are overlain. Contour interval: thin red contour  $0.25 \text{ Pa s}^{-1}$ , thick contours begin at  $0.5 \text{ Pa s}^{-1}$  and increase in intervals of  $0.5 \text{ Pa s}^{-1}$ . Red contours for ascent, blue contours for descent.

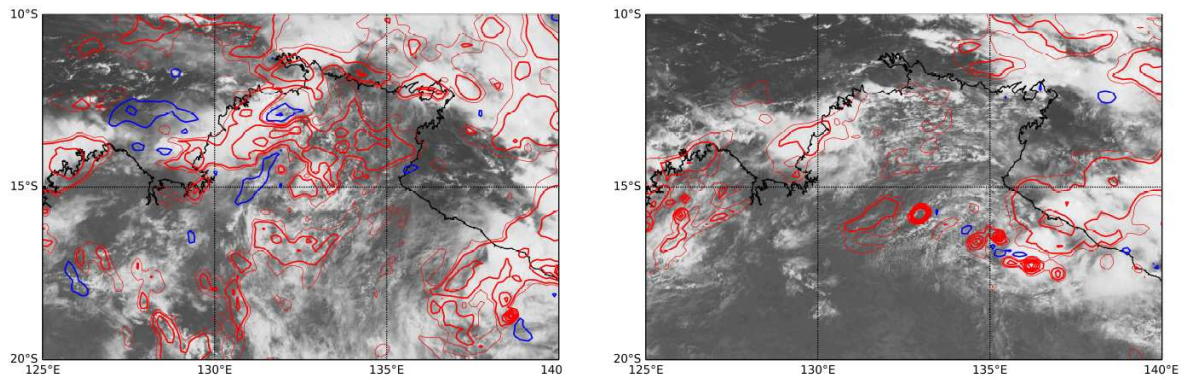
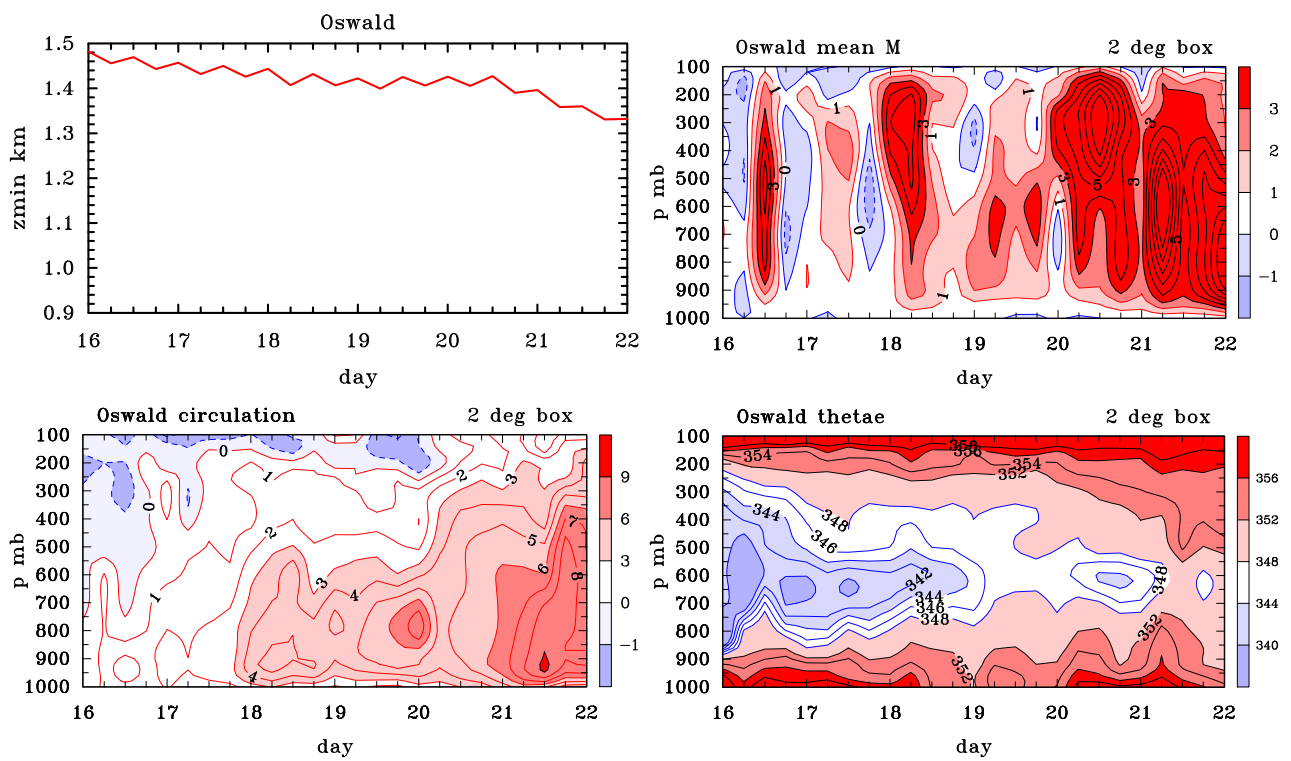


Figure 20 (a) Time series of minimum geopotential at 850 mb for the low that became tropical cyclone Oswald. Time-height cross-section of system averaged quantities within (or in the case of (c) around) a box  $2^\circ\text{lon} \times 2^\circ\text{lat}$ , centred on the location of the minimum geopotential at 850 mb. These include (b) the vertical mass flux per unit area (units  $\text{kg m}^{-2} \text{s}^{-1}$ ), (c) the normalized circulation around the box (units  $\text{m s}^{-1}$ ), and (d) the pseudo-equivalent potential temperature (in K).



The foregoing summary is consistent with the findings of Tory et al. (2006a,b, 2007), who considered three aspects of vortex spin up, (i) the direct spin up of cyclonic vorticity anomalies in convective bursts, (ii) the accumulation of such anomalies into a monolithic vortex core, and (iii) the amplification of the system-scale vorticity associated with the convectively driven system-scale secondary circulation, which they termed the system-scale intensification. In this paper the availability of data at a minimum of 6 hourly intervals does not permit a study of the first two processes. Thus, in contrast to Tory *et al.*'s focus on vorticity enhancement mechanisms, we focus here on the spin up of the system-scale tangential wind.

We have not investigated what the earlier Tory et al. papers describe as the progressive amalgamation of convectively-generated patches of enhanced low level vorticity to form a vortex monopole. While this process is evident also in the ECMWF analyses, the temporal resolution of the analyses (6 h) is too coarse to be able to follow individual patches of vorticity with certainty. Even though the amalgamation of vorticity does not by itself account for the circulation changes around fixed circuits encircling the vorticity patches, we still regard it as an important element of the vorticity organization and upscale cascade process.

While forecasters on the bench do not usually examine vorticity fields as part of the forecast process, we suggest that vorticity and related analyses of the type examined here may provide a useful framework for *understanding* the dynamics of tropical low formation within the broader-scale monsoon circulation and for interpreting model forecasts.

## Conclusions

We have presented an analysis of tropical low formation in the Australian monsoon during January 2013 based on European Centre for Medium Range Weather Forecast analyses. In particular, we examined three lows that all developed on the monsoon shear line, two of which eventually became tropical cyclones. One of the lows intensified as it made a loop over land. Interpretations of the formation were given in terms of vorticity dynamics and these interpretations apply to developments over the land as well as over the sea. In both developing cases, the analyses indicate that the intensification of the low requires periodic bursts of deep convection near the centre of the gyre to promote the further concentration of vorticity near the centre. This concentration of vorticity increases the local circulation about the centre, which amounts to increasing the local tangential wind speed and, through approximate gradient wind balance above the boundary layer, to a lowering of the central pressure. While there is a number of regions of elevated vorticity coinciding with deep convection in the monsoon trough, the intensification of a tropical low occurs only in a region of locally-enhanced Okubo-Weiss parameter. The results of this limited study suggest that the processes by which tropical lows form over land are *not* fundamentally different from those of tropical lows that form over the sea. Further cases are being examined currently and the results of these studies will be presented in due course.

## Acknowledgements

We thank Dr. Martin Miller for suggesting the utility of the ECMWF analyses for process studies of the type described here. This work was motivated by numerous visits by the first two authors to the Australian Bureau of Meteorology's Regional Forecast Centre in Darwin during the monsoon season and the opportunity these visits provided to witness the monsoon first hand as well as the forecasting challenges it poses. We thank a series of Regional Directors over the years for their warm hospitality and support for our research: they include Jim Arthur, Geoffrey Garden, Andrew Tupper and Todd Smith. We thank also the many forecasters at the Regional Office who have shared their expertise with us. We thank Denis Margetic from the Bureau of Meteorology Head Office for supplying us with satellite data and for code to plot these data. Finally we thank Michael Reeder, Kevin Tory and Hongyan Zhu for their insightful reviews of the original version of the manuscript.

RKS acknowledges funding for tropical cyclone research from the German Research Council (Deutsche Forschungsgemeinschaft) under Grant no SM30/23-4 and the Office of Naval Research Global under Grant No. N62909-15-1-N021. MTM acknowledges the support of NSF grant AGS-1313948, NOAA HFIP grant N0017315WR00048, NASA grant NNG11PK021 and the U.S. Naval Postgraduate School.

## Appendix: The Okubo-Weiss parameter

The OW parameter is defined here by  $OW = Re[\zeta^2 - D^2 - S^2 - 2|D|\sqrt{S^2 - \zeta^2}]$ , where

$$\zeta = \frac{1}{R \cos \theta} \left( \frac{\partial v}{\partial \lambda} - \frac{\partial u \cos \theta}{\partial \theta} \right), \quad (2)$$

is the vertical component of relative vorticity,

$$D = \frac{1}{R \cos \theta} \left( \frac{\partial v \cos \theta}{\partial \theta} + \frac{\partial u}{\partial \lambda} \right), \quad (3)$$

is the horizontal divergence,  $S^2 = E^2 + F^2$  is the square of the total deformation (or strain),  $E$  and  $F$  are the stretching and shear deformation rates given by,

$$E = \frac{1}{R \cos \theta} \frac{\partial u}{\partial \lambda} - \frac{\cos \theta}{R} \frac{\partial}{\partial \theta} \left( \frac{v}{\cos \theta} \right) \quad (4)$$

and

$$F = \frac{1}{R \cos \theta} \frac{\partial v}{\partial \lambda} + \frac{\cos \theta}{R} \frac{\partial}{\partial \theta} \left( \frac{u}{\cos \theta} \right), \quad (5)$$

$\lambda$  is the longitude,  $\theta$  is the latitude and  $R$  is the radius of the Earth (Batchelor 1967; Lukovich and Barber 2009). The foregoing definition of OW is the un-approximated form, unlike that used by Dunkerton et al. (2009), who used a  $\beta$ -plane representation omitting the effects of divergence, and Tory et al. (2013) who proposed a normalized form of the approximation without divergence to facilitate easy recognition of regions of near solid body rotation. Originally we used the simplified form of OW as in Dunkerton et al. (2009), but the data to compute the full form were available and so we used these. It turned out, however, that the differences in the OW patterns were generally small.

## References

- Batchelor, G.K. 1967. An introduction to fluid dynamics. Cambridge University Press, Cambridge, England, 615pp.
- Bauer, P., Auligné, T., Bell, W., Geer, A., Guidard, V., Heilliette, S., Kazumori, M., Kim, M.J., Liu, E.H.C., McNally, A.P., Macpherson, B., Okamoto, K., Renshaw, R., and Riishøjgaard, L.P. 2011. Satellite cloud and precipitation assimilation at operational NWP centres. *Quart. J. Roy. Met. Soc.*, 137, 1934–1951.
- Davidson, N.E. and Holland, G.H. 1987. A diagnostic analysis of two intense monsoon depressions over Australia. *Mon. Wea. Rev.*, 115, 380–392.
- Dunkerton, T.J., Montgomery, M.T., and Wang, Z. 2009. Tropical cyclogenesis in a tropical wave critical layer: easterly waves. *Atmos. Chem. Phys.*, 9, 5587–5646.
- Ferreira, R.N. and Schubert, W.H. 1997. Barotropic aspects of ITCZ breakdown. *J. Atmos. Sci.*, 54, 261–285.
- Foster, I.J. and Lyons, T.J. 1984. Tropical cyclogenesis: A comparative study of two depressions in the northwest of Australia. *Quart. J. Roy. Met. Soc.*, 110, 105–119.
- Haynes, P. and McIntyre, M.E. 1987. On the evolution of vorticity and potential vorticity in the presence of diabatic heating and frictional or other forces. *J. Atmos. Sci.*, 44, 828–841.
- Hendricks, E.A., Montgomery, M.T., and Davis, C.A. 2004. On the role of “vortical hot towers” in the formation of tropical cyclone Diana (1984). *J. Atmos. Sci.*, 61, 1209–1232.
- Holton, J.R. 2004. An introduction to dynamic meteorology, Fourth Edition. Academic Press, London, 535pp.
- Kilroy, G. and Smith, R.K. 2013. A numerical study of rotating convection during tropical cyclogenesis. *Quart. J. Roy. Met. Soc.*, 139, 1255–1269.
- Lukovich, J.V. and Barber, D.G. 2009. On horizontal wind gradient variability from the stratosphere to the lower troposphere in the Arctic. *J. Geophys. Res.*, 114. . D02104.
- McBride, J.L. and Keenan, T.D. 1982. Climatology of tropical cyclone genesis in the Australian region. *J. Clim.*, 2, 13–33.
- Montgomery, M.T., Davis, C., Dunkerton, T., Wang, Z., Velden, C., Torn, R., Majumdar, S., Zhang, F., Smith, R.K., Bosart, L., Bell, M.M., Haase, J.S., Heymsfield, A., Jensen, J., Campos, T., and Boothe, M.A. 2012. The Pre-Depression Investigation of Cloud systems in the Tropics (PREDICT) experiment: Scientific basis, new analysis tools, and some first results. *Bull. Amer. Meteor. Soc.*, 93, 153–172.
- Montgomery, M.T., Nicholls, M.E., Cram, T.A., and Saunders, A. 2006. A “vortical” hot tower route to tropical cyclogenesis. *J. Atmos. Sci.*, 63, 355–386.

- Montgomery, M.T. and Smith, R.K. 2014. Paradigms for tropical cyclone intensification. *Aust. Met. Oceanogr. J.*, 64, 37–66.
- Raymond, D.J., Gjorgjievska, S., Sessions, S.L., and Fuchs, Z. 2014. Tropical cyclogenesis and mid-level vorticity. *Aust. Met. Oceanogr. J.*, 64, 11–25.
- Raymond, D.J. and Lopez-Carillo, C. 2011. The vorticity budget of developing Typhoon Nuri (2008). *Atmos. Chem. Phys.*, 11, 147–163.
- Smith, R.K. and Montgomery, M.T. 2015. Towards clarity on tropical cyclone intensification. *J. Atmos. Sci.*, 72, 3020–3031.
- Tory, K.J., Dare, R.A., Davidson, N.E., McBride, J.L., and Chand, S.S. 2013. The importance of low-deformation vorticity in tropical cyclone formation. *Atmos. Chem. Phys.*, 13, 2115–2132.
- Tory, K.J., Davidson, N.E., and Montgomery, M.T. 2007. Prediction and diagnosis of tropical cyclone formation in an NWP system. Part III: Diagnosis of developing and nondeveloping storms. *J. Atmos. Sci.*, 64, 3195–3213.
- Tory, K.J., Kepert, J.D., Sippel, J.A., and Nguyen, C.M. 2012. On the use of potential vorticity tendency equations for diagnosing atmospheric dynamics in numerical models. *J. Atmos. Sci.*, 69, 942–960.
- Tory, K.J., Montgomery, M.T., and Davidson, N.E. 2006a. Prediction and diagnosis of tropical cyclone formation in an NWP system. Part I: The critical role of vortex enhancement in deep convection. *J. Atmos. Sci.*, 63, 3077–3090.
- Tory, K.J., Montgomery, M.T., Davidson, N.E., and Kepert, J.D. 2006b. Prediction and diagnosis of tropical cyclone formation in an NWP system. Part II: A detailed diagnosis of tropical cyclone formation. *J. Atmos. Sci.*, 63, 3091–3113.
- Wang, Z., Montgomery, M.T., and Fritz, C. 2012. A first look at the structure of the wave pouch during the 2009 PREDICT-GRIP dry runs over the atlantic. *Mon. Wea. Rev.*, 140, 1144–1163.